Engineered Interphase Mechanics in Single Lap Joints: Analytical and PINN Formulations

P. R. Budarapu[*,‖], S. Kumar[†], M. A. Khan[‡], B. Rammohan[‡] and and C. Anitescu[¶]

[*]*School of Mechanical Sciences, Indian Institute of Technology Bhubaneswar 752050, India*

[†]*James Watt School of Engineering, Oakfield Avenue University of Glasgow, G12 8LT, United Kingdom*

[‡]*Department of Civil Engineering Mahindra University École Centrale School of Engineering Hyderabad 500043, India*

[§]*Dayananda Sagar University (DSU) Kudlu Gate Campus, Bangalore 560114, India*

[¶]*Institute of Structural Mechanics Bauhaus University of Weimar 99423 Weimar, Germany*

[‖]*pattabhi@iitbbs.ac.in*

Received
Accepted
Published

Adhesively bonded joints showcase non-uniform stress distribution, along their length as the load is transferred through layers of dissimilar stiffness. For efficient transfer of loads, the peak interfacial shear stress is required to be engineered. In this study, inspired by electric pulses, the interphase modulus is modified according to square, sinusoidal and triangular pulses. The variation in peak stresses with increased number of pulses up to four is also investigated. The developed analytical model is solved for the interfacial shear stresses as well as the peel stresses, using energy functional approach, through MAPLE software. The abrupt changes in modulus in square pulse graded interphase are observed to create highest interfacial shear stresses among the considered grading profiles. Furthermore, the peak interfacial stresses are observed to increase with increased number of pulses. An effective elastic modulus parameter is defined to indicate the area under the modulus profile curve. The effective modulus is found to be gradually increasing with increase number of pulses in square graded interphase. Whereas, it is constant for sinusoidal- and triangular-graded interphases. A deep machine learning-based physics informed neural network model is developed to quickly solve the developed governing differential equations. Therefore, results from the machine leaning model are compared to the analytical results.

Keywords: Single lap joint; engineered interphase; interfacial shear stress; square, sinusoidal and triangular pulses; physics informed neural networks; loss function.

[*]Corresponding author.

1. Introduction

Adhesively bonded joints are a class of multi-material systems which characteristically showcase non-uniform stress distribution, along their length as the load is transferred through layers of dissimilar stiffnesses. Other class of systems where a stress solution proposed for an adhesively bonded joint could be applicable include: structural/composite repairs [Khan and Kumar (2017)], interfacial stress transfer through fiber and matrix in a composite [Pal and Kumar (2016); Budarapu *et al.* (2019); Dusane *et al.* (2021)], integrated circuit chips bonded to a substrate [Yacobi *et al.* (2002); Sutrakar *et al.* (2021)].

In general, the load transfer in adhesively bonded assemblies is associated with characteristic peak stresses. These characteristic peaks could be alleviated by the use of materially-tailored/engineered adhesive and/or adherend. A framework was proposed in [Budarapu *et al.* (2020)] to design nacre-inspired composites incorporating a functionally modulus-graded interphase material. The stress analyses of the flat and the circular bonded assemblies in the presence of a materially-tailored adhesive/adherends showed the mitigation of peak stress concentration in [Kumar (2009); Khan *et al.* (2018); Khan and Kumar (2018); Stein *et al.* (2016); Ubaid *et al* (2018)]. Tapering of the adherends' near the edges was also utilized to tailor the stiffness of the bonded joints in order to reduce the peak stresses [Oterkus *et al.* (2006)].

The proposed study utilizes material tailoring of the adhesive interface as an approach to reduce the peak stresses for single lap bonded joints. In agreement with the authors' previous studies, [Kumar (2009); Khan *et al.* (2018)], the modulus profile of the adhesive is engineered such that it has the lowest value at the ends where the peak stress concentrations exist. The effective redistribution of stresses leads to an improved performance of the system in terms of strength and toughness, as seen in [Khan and Kumar (2018)]. The bondline could be engineered to achieve tailored properties using several methods such as (i) controlling the curing kinetics of the adhesive [Carbas *et al.* (2014)], (ii) selectively reinforcing the adhesive with nano-reinforcement [Stapleton *et al.* (2012); Carbas *et al.* (2017)], (iii) depositing adhesive with varying stiffness via three-dimensional (3D) printing [Kumar *et al.* (2017); Khan and Kumar (2018)], (iv) use of robot to dispense the adhesives in required graded ratios [Kawasaki *et al.* (2016)], to name a few.

A number of published studies focused on developing theoretical, numerical and experimental approaches to evaluate the performance of the adhesively bonded joints/multi-layer assemblies with/without an engineered adhesive. For instance, a numerical study, utilizing finite element discretization, was employed to perform the analysis of orthotropic multilayered beams while adequately accounting for variations in through thickness stresses [Van Pham *et al.* (2018)]. The experimental evaluation of the joints with engineered interfaces was discussed before. However, the focus of this study is to utilize Physics Inspired Neural Networks (PINN) to solve

the governing differential equations obtained from an analytical approach [Goswami *et al.* (2020); Sharma *et al.* (2021); Varma *et al.* (2022)]. Initial analytical studies could be found in the proponent works of [Goland and Reissner (1944); Hart-Smith (1973); Lubkin and Reissner (1955)].

A deep collocation method considering computational graphs and backpropagation algorithms involved in deep learning, aimed at solving thin plate bending problems is proposed in [Hongwei Guo and Rabczuk (2019)]. A method for solving partial differential equations using artificial neural networks and an adaptive collocation strategy is discussed in [Anitescu *et al.* (2019); Samaniego *et al.* (2020)]. A deep autoencoder-based energy method to perform the bending, vibration and buckling analysis of Kirchhoff plates is discussed in [Zhuang *et al.* (2021)]. On the other hand, a neural architecture search and transfer learning-based stochastic deep collocation method for heterogeneous porous media is introduced in [Guo *et al.* (2022)]. A neural network-based deep energy approach to solve applied elasticity problems considering strain gradient effects is highlighted in [Nguyen-Thanh *et al.* (2021)].

The main objective of this study is to investigate the stress distribution in a single lap joint considering a variety of interphases with varying elastic modulus. An analytical model considering the materials, geometry, loads and boundary conditions is developed to estimate the interfacial shear stresses and peel stresses in a single lap joint (SLJ). The developed analytical model involves complex fourth-order differential equations, which becomes cumbersome when the variation of elastic modulus is also considered. Therefore, the analytical expressions are solved using MAPLE(R). The studies are further extended to investigate the influence of thickness of the interphase and the adherend on the stress distribution. On the other hand, the complex analytical equations can be efficiently solved by employing artificial neural networks. Therefore, a physics informed neural network (PINN) model is proposed to solve for the interfacial shear stresses. Results estimated using the proposed analytical model are validated with the results from the proposed PINN model as well as a numerical model developed in ABAQUS. Therefore, the novelties of this study are (i) The creation of a novel interphase grading profiles, like: square, sinusoidal and triangular pulses, to tailor the elastic modulus of the interphase. (ii) Solution techniques to solve the developed governing differential equations via MAPLE software. (iii) Development of physics informed neural networks-based deep machine learning models to solve the governing differential equations of a single lap joint.

This paper is arranged as follows. Details of the analytical model along with the modulus grading profiles are explained in Sec. 2. The influences of the domain length, grading profile, tablet thickness, interphase thickness on the peak interfacial shear stresses and the variation of the peel stresses are discussed in Sec. 3. The PINN model is introduced in Sec. 4. Key findings are summarized in Sec. 5.

2. Modeling Aspects

In this section, development of an analytical model to estimate the axial, shear and peel stresses in single lap joints is presented. Furthermore, potential energy-based approach by defining an energy functional, combined with the Lagrangian equations of motion is adopted to solve for the stresses in single lap joints. The developed methodology is further extended considering variation of elastic modulus according to square, sinusoidal and triangular laws.

2.1. *Analytical model*

Consider a single lap joint as shown in Fig. 1, where two tablets of length L and height h_1 and h_2 are adhered together by an adhesive of length L and height h. The origin of the coordinate system is placed at the lower left corner. The distances of the top of bottom tablet, matrix and top tablet from the bottom surface are denoted by b, c and d, respectively. Let the right edge of the top tablet be subjected to a uni-axial tensile load σ_0, such that the reaction force on the left edge of the bottom tablet is given by $\rho\sigma_0$, where $\rho = \frac{h_1}{h_2}$.

Let the normal stresses along the x and y directions be denoted by $\sigma_x^{(i)}$ and $\sigma_y^{(i)}$, respectively, and the shear stresses by $\sigma_{xy}^{(i)}$; where the superscript i indicates the constituent: $i = 1$, 2 and 3 represent the top tablet, interphase and the bottom tablet, respectively, see Fig. 1. Therefore, the equilibrium equations can be written as [Ajayan *et al.* (2003)]

$$\frac{\partial \sigma_x^{(i)}}{\partial x} + \frac{\partial \tau_{xy}^{(i)}}{\partial y} = 0, \tag{1a}$$

$$\frac{\partial \tau_{xy}^{(i)}}{\partial x} + \frac{\partial \sigma_y^{(i)}}{\partial y} = 0. \tag{1b}$$

Combining the governing equation (1) and the boundary conditions in Eq. (A.1), after denoting $\sigma_x^{(1)} = \sigma_1$ and $\sigma_x^{(2)} = \sigma_2$, the normal and shear stress components can be expressed as

$$\sigma_y^{(1)} = \frac{1}{2}(d-y)^2\sigma_1'', \tag{2a}$$

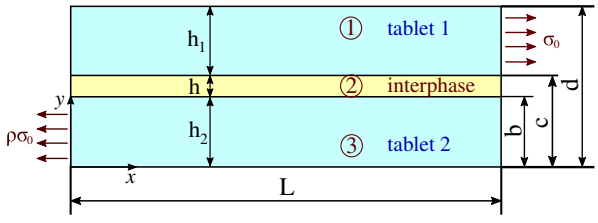

Fig. 1. Schematic of a single lap joint, highlighting two tablets adhered together by an interphase. The right edge of the top tablet is subjected to a uni-axial tensile load σ_0, such that the reaction force on the left edge of the bottom tablet is equal to $\rho\sigma_0$.

$$\tau_{xy}^{(1)} = (d-y)\sigma_1', \tag{2b}$$

$$\sigma_y^{(2)} = \frac{1}{2}(c-y)^2\sigma_2'' + h_1\left(c-y+\frac{h_1}{2}\right)\sigma_1'', \tag{2c}$$

$$\tau_{xy}^{(2)} = (c-y)\sigma_2' + h_1\sigma_1', \tag{2d}$$

$$\sigma_y^{(3)} = \frac{1}{2}[(y^2-b^2)\sigma_3'' + h^2\sigma_2'' + (2h_1h+h_1^2)\sigma_1''], \tag{2e}$$

$$\tau_{xy}^{(3)} = -\sigma_3' y. \tag{2f}$$

Furthermore, considering the force equilibrium, the axial stress in the interphase is given by

$$\sigma_2 = \alpha_1(\sigma_0 - \sigma_1) - \alpha_2\sigma_3, \tag{3}$$

where $\alpha_1 = \frac{h_1}{h}$ and $\alpha_2 = \frac{h_2}{h}$, see Eq. (A.2) for further details. Therefore, the axial stresses σ_1, σ_2 and σ_3 are estimated by considering the potential energy of the system

$$\Pi^* = \frac{1}{2}\int_0^L \int_y [\sigma_x^{(i)} \quad \sigma_y^{(i)} \quad \tau_{xy}^{(i)}] \begin{bmatrix} \epsilon_x^{(i)} \\ \epsilon_y^{(i)} \\ \gamma_{xy}^{(i)} \end{bmatrix} dxdy, \tag{4}$$

where

$$\begin{bmatrix} \epsilon_x^{(i)} \\ \epsilon_y^{(i)} \\ \gamma_{xy}^{(i)} \end{bmatrix} = \begin{bmatrix} \frac{1}{E_x^{(i)}} & \frac{-\nu_{xy}^{(i)}}{E_y^{(i)}} & 0 \\ \frac{-\nu_{yx}^{(i)}}{E_x^{(i)}} & \frac{1}{E_y^{(i)}} & 0 \\ 0 & 0 & \frac{1}{2G_{xy}^{(i)}} \end{bmatrix} \begin{bmatrix} \sigma_x^{(i)} \\ \sigma_y^{(i)} \\ \tau_{xy}^{(i)} \end{bmatrix} + \begin{bmatrix} \alpha_x^{(i)} & 0 & 0 \\ 0 & \alpha_y^{(i)} & 0 \\ 0 & 0 & 0 \end{bmatrix} \Delta T. \tag{5}$$

Therefore, after substituting Eq. (5) into Eq. (4), we have

$$\Pi^* = \frac{1}{2}\int_0^L \int_y \left[\sigma_x^{(i)}\left(\frac{\sigma_x^{(i)}}{E_x^{(i)}} - \sigma_y^{(i)}\frac{\nu_{xy}^{(i)}}{E_y^{(i)}} + \alpha_x\Delta T\right) + \sigma_y^{(i)}\left(-\sigma_x^{(i)}\frac{\nu_{yx}^{(i)}}{E_x^{(i)}} + \frac{\sigma_y^{(i)}}{E_y^{(i)}} + \alpha_y\Delta T\right) + \tau_{xy}^{(i)}\left(\frac{\tau_{xy}^{(i)}}{2G_{xy}^{(i)}}\right)\right] dxdy. \tag{6}$$

Equation (6) can be simplified by considering that (i) the thermal stresses are neglected, $\Delta T = 0$, (ii) Poisson's ratio is constant in all directions, $\nu_{xy}^{(i)} = \nu_{yx}^{(i)} = \nu^{(i)}$ and (iii) the material is isotropic such that Young's modulus is same along the x and y directions, $E_x^{(i)} = E_y^{(i)} = E^{(i)}$. Therefore, simplified form of Eq. (6) is given by

$$\begin{aligned}\Pi^* = \frac{1}{2}\int_0^L \int_y \Bigg[& \frac{1}{E^{(1)}}(\sigma_1\sigma_1 + \sigma_y^{(1)}\sigma_y^{(1)} - 2\nu^{(1)}\sigma_1\sigma_y^{(1)} + (1+\nu^{(1)})\tau_{xy}^{(1)}\tau_{xy}^{(1)}) \\ & + \frac{1}{E^{(2)}}(\sigma_2\sigma_2 + \sigma_y^{(2)}\sigma_y^{(2)} - 2\nu^{(2)}\sigma_2\sigma_y^{(2)} + (1+\nu^{(2)})\tau_{xy}^{(2)}\tau_{xy}^{(2)}) \\ & + \frac{1}{E^{(3)}}(\sigma_3\sigma_3 + \sigma_y^{(3)}\sigma_y^{(3)} - 2\nu^{(3)}\sigma_3\sigma_y^{(3)} + (1+\nu^{(3)})\tau_{xy}^{(3)}\tau_{xy}^{(3)}) \Bigg] dxdy. \end{aligned} \tag{7a}$$

Substituting Eqs. (2) and (3) in Eq. (7), the system potential energy becomes

$$\begin{aligned}\Pi^* = \int_0^L \Bigg[& \left(\frac{h_1^5}{40E_1} + \frac{h_1^2(4h^3 + 3hh_1^2 + 6h_1h^2)}{24E_2} + \frac{b(2h_1h + h_1^2)^2}{8E_3}\right)\sigma_1''^2 \\ & + \left(\frac{h^5}{40E_2} + \frac{bh^4}{8E_3}\right)\sigma_2''^2 + \frac{b^5}{15E_3}\sigma_3''^2 + \left(\frac{h_1(4ch^3 - c^4 + 3b^4 + 6c^2b^2 - 8cb^3)}{24E_2}\right. \\ & \left. + \frac{bh^2(2h_1h + h_1^2)}{4E_3}\right)\sigma_1''\sigma_2'' - \frac{b^3h^2}{6E_3}\sigma_2''\sigma_3'' - \frac{b^3(2h_1h + h_1^2)}{6E_3}\sigma_1''\sigma_3'' - \frac{\nu_1 h_1^3}{6E_1}\sigma_1''\sigma_1 \\ & - \frac{\nu_2 h^3}{6E_2}\sigma_2''\sigma_2 - \frac{\nu_2 h_1(2ch - c^2 + b^2 + hh_1)}{2E_2}\sigma_1''\sigma_2 - \frac{\nu_3 bh^2}{2E_3}\sigma_2''\sigma_3 \\ & - \frac{\nu_3 b(2h_1h + h_1^2)}{2E_3}\sigma_1''\sigma_3 + \frac{2\nu_3 b^3}{6E_3}\sigma_3''\sigma_3 + \left(\frac{(1+\nu_1)h_1^3}{6E_1} + \frac{(1+\nu_2)hh_1^2}{2E_2}\right)\sigma_1'^2 \\ & + \frac{(1+\nu_2)h^3}{6E_2}\sigma_2'^2 + \frac{(1+\nu_3)b^3}{6E_3}\sigma_3'^2 + \frac{(1+\nu_2)h^2h_1}{2E_2}\sigma_1'\sigma_2' + \frac{h_1}{2E_1}\sigma_1^2 \\ & + \frac{h}{2E_2}\sigma_2^2 + \frac{b}{2E_3}\sigma_3^2\Bigg] dx. \end{aligned} \tag{8a}$$

Let the energy functional Ψ be defined as

$$\begin{aligned}\Psi = & A_1\sigma_1''^2 + A_2\sigma_2''^2 + A_3\sigma_3''^2 + A_4\sigma_1''\sigma_2'' + A_5\sigma_2''\sigma_3'' + A_6\sigma_1''\sigma_3'' + A_7\sigma_1''\sigma_1 \\ & + A_8\sigma_2''\sigma_2 + A_9\sigma_1''\sigma_2 + A_{10}\sigma_2''\sigma_3 + A_{11}\sigma_1''\sigma_3 + A_{12}\sigma_3''\sigma_3 + A_{13}\sigma_1'^2 \\ & + A_{14}\sigma_2'^2 + A_{15}\sigma_3'^2 + A_{16}\sigma_1'\sigma_2' + A_{17}\sigma_1^2 + A_{18}\sigma_2^2 + A_{19}\sigma_3^2, \end{aligned} \tag{9a}$$

where the constants A_1 to A_{19} indicate the coefficients of the corresponding terms in the integrand of Eq. (8), mentioned through Eq. (A.3). Using Eq. (A.2)(b–f),

Eq. (9) can be rearranged as

$$\begin{aligned}\Psi = {} & A_1\sigma_1''^2 + A_2(\alpha_1\sigma_1'' + \alpha_2\sigma_3'')^2 + A_3\sigma_3''^2 + A_4\sigma_1''(-\alpha_1\sigma_1'' - \alpha_2\sigma_3'') \\ & + A_5(-\alpha_1\sigma_1'' - \alpha_2\sigma_3'')\sigma_3'' + A_6\sigma_1''\sigma_3'' + A_7\sigma_1''\sigma_1 + A_8(-\alpha_1\sigma_1'' - \alpha_2\sigma_3'') \\ & \times [\alpha_1(\sigma_0 - \sigma_1) - \alpha_2\sigma_3] + A_9\sigma_1''[\alpha_1(\sigma_0 - \sigma_1) - \alpha_2\sigma_3] + A_{10}(-\alpha_1\sigma_1'' - \alpha_2\sigma_3'')\sigma_3 \\ & + A_{11}\sigma_1''\sigma_3 + A_{12}\sigma_3''\sigma_3 + A_{13}\sigma_1'^2 + A_{14}(\alpha_1\sigma_1' + \alpha_2\sigma_3')^2 \\ & + A_{15}\sigma_3'^2 + A_{16}\sigma_1'(-\alpha_1\sigma_1' - \alpha_2\sigma_3') + A_{17}\sigma_1^2 + A_{18}[\alpha_1(\sigma_0 - \sigma_1) - \alpha_2\sigma_3]^2 \\ & + A_{19}\sigma_3^2. \end{aligned} \tag{10a}$$

The unknown axial stresses σ_1 and σ_3 can be estimated by considering Lagrange's equations of motion of the energy functional in Eq. (10), shown as follows:

$$\frac{d^2}{dx^2}\left(\frac{\partial\Psi}{\partial\sigma_i''}\right) - \frac{d}{dx}\left(\frac{\partial\Psi}{\partial\sigma_i'}\right) + \frac{\partial\Psi}{\partial\sigma_i} = 0, \quad \text{where } i = 1 \text{ or } 3. \tag{11}$$

When $i = 1$, Eq. (11) becomes

$$B_1\sigma_1'''' + B_2\sigma_3'''' + B_3\sigma_1'' + B_4\sigma_3'' + B_5\sigma_1 + B_6\sigma_3 + B_7 = 0, \tag{12}$$

where the coefficients B_1 to B_7 are mentioned in Eq. (A.4). Similarly, when $i = 3$, Eq. (11) transforms to

$$C_1\sigma_1'''' + C_2\sigma_3'''' + C_3\sigma_1'' + C_4\sigma_3'' + C_5\sigma_1 + C_6\sigma_3 + C_7 = 0, \tag{13}$$

where the coefficients C_1 to C_7 are listed in Eqs. (A.5). Equations (12) and (13) are solved for the axial stresses σ_1 and σ_3 with the help of MAPLE(R). Therefore, the axial stress in the interphase σ_2 can be estimated using Eq. (3). After knowing the axial stresses, the shear (τ_{xy}) and peel (σ_y) stresses in each of the constituents are estimated using Eq. (2).

2.2. *Modulus graded interphase*

The mechanics of stress transfer across the interphase are studied by varying the elastic modulus of the interphase. For smooth transfer of stresses, soft interphase properties are preferred towards the edges. This is because the peak possible load transfer depends on the maximum shear stress prevailing in the SLJ. The maximum shear stresses usually occur at the edges. A stiff interphase with large elastic modulus results in poor load transfer, leading to failure of the interphase in a brittle fashion. On the other hand, a soft interphase results in smooth transfer of small amplitude loads. Therefore, a graded interphase with stiff modulus in the middle of the domain and smooth modulus towards the edges is an ideal combination for smooth transfer of large amplitude loads. In this study, the elastic modulus is graded based on the square, sinusoidal and triangular law pulses, as shown in Fig. 2.

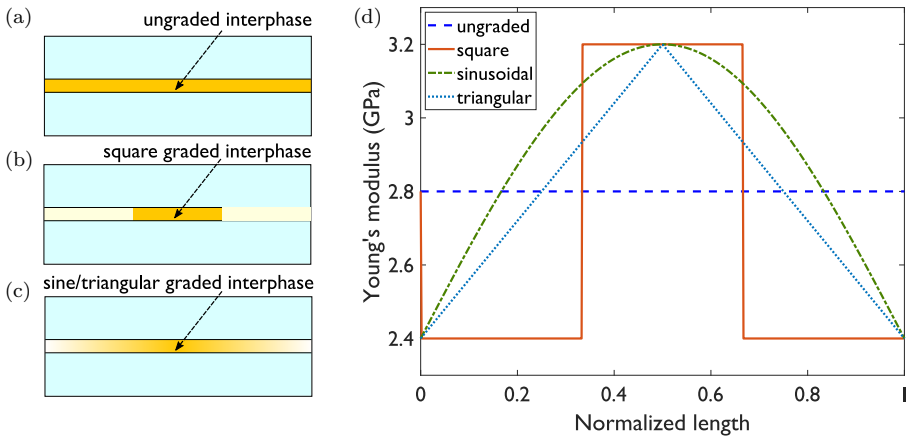

Fig. 2. Schematic of a single lap joint containing an interphase with (a) uniform elastic modulus, and elastic modulus varying according to (b) a square pulse and (c) sinusoidal and triangular pulses. The corresponding variation of the interphase modulus along the domain length is shown in (d).

The selected grading laws are inspired by signals in electrical engineering. As shown in Fig. 2, the elastic modulus is maximum at the center of the domain and minimum towards the edges. Furthermore, according to Fig. 2(d), the elastic modulus abruptly changes in case of square pulse. Whereas, the change is smooth and linear in sinusoidal and triangular pulses, respectively. In this study, the mean value of the interphase modulus is adopted to be 2.8 GPa, whereas the minimum and maximum values are given by 2.4 GPa and 3.2 GPa, respectively. In this context, we define the effective modulus as the area under under Young's modulus versus domain length curve. According to Fig. 2(d), Young's modulus is constant throughout the domain length in case of ungraded interphase. Therefore, its effective modulus (E_{eff}) is equal to 2800 N/m. In the similar lines, the effective elastic modulus of the interphase considering square, sinusoidal and triangular laws, with varying number of pulses is provided in Table 1.

According to Table 1, the effective modulus varies only in case of square pulse, which is observed to increase with increase in number of pulses. This is due to its unsymmetrical distribution. Furthermore, E_{eff} is the highest for sinusoidal pulse,

Table 1. Effective elastic modulus of the interphase considering square, sinusoidal and triangular laws, with varying number of pulses.

Number of Pulses	Effective elastic modulus of the interphase ($\times 10^3$ N/m)			
	Ungraded	Square pulse	Sinusoidal pulse	Triangular pulse
single	2.8	3.04	3.62	3.36
two	2.8	3.17	3.62	3.36
three	2.8	3.23	3.62	3.36
four	2.8	3.25	3.62	3.36

followed by triangular and square pulses and is the lowest for ungraded interphase. Therefore, the peak interfacial stresses can be expected to be lowest in the SLJ with modulus graded according to sinusoidal pulse, followed by triangular and square pulses and highest for the SLJ with ungraded interphase.

2.2.1. *Square pulse graded interphase*

The variation of elastic modulus according to a square pulse along the domain length can be estimated by

$$E_2 = E_{\text{mean}} + (E_{\text{mean}} - E_{\text{max}})\text{sign}\left[\sin\left(\frac{n\pi x}{L}\right)\right], \tag{14}$$

where E_{mean} and E_{max} indicate the mean and maximum values of the interphase modulus, "sign" denotes the sign function, and n represents the total number of peaks and troughs in a given square pulse. For example, in a single square pulse, one peak and two troughs are noticed, yielding n equal to 3, Fig. 2(b) and in case of two square pulses, two peaks and three troughs are observed, resulting in n equal to 5 and so on. The particular pattern is selected to ensure that the interphase modulus is always minimum at the edges.

Variation of the interphase elastic modulus according to single, two and four square pulses is shown in Figs. 2(d), 3(a) and 3(b), respectively. When the elastic modulus of the interphase varies according to single square pulse along the domain length, see Figs. 2(b) and 2(d), it will be changing in patches. This means in a single square pulse, the modulus will be minimum until one third length of the domain, followed by the maximum elastic modulus for the next one-third length and minimum modulus in the last one-third length of the domain, see Figs. 2(b) and 2(d). In the similar lines, when the elastic modulus varies according to two and four square pulses, the alternate minimum-maximum pattern will be repeating, as

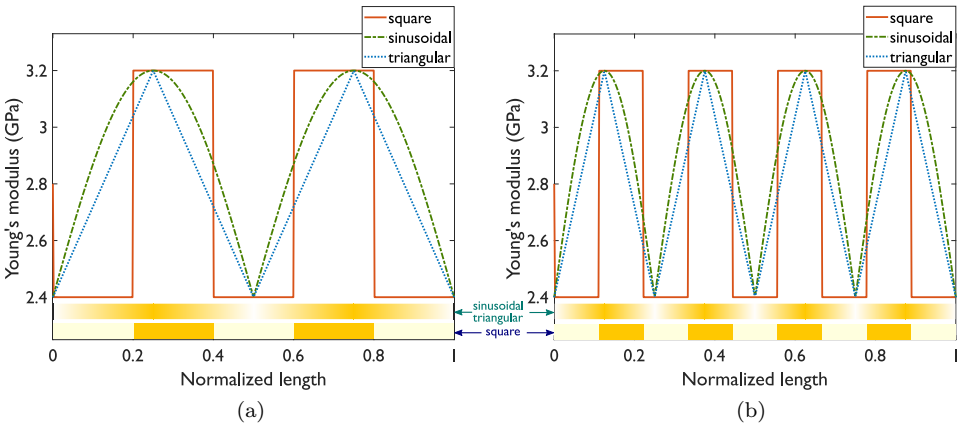

Fig. 3. Variation of elastic modulus along the interphase in a single lap joint, considering (a) two and (b) four; square, sinusoidal and triangular pulses.

shown in Fig. 3. Hence, abrupt changes in interphase modulus occur when the variation is according to a square pulse.

2.2.2. *Sinusoidal pulse-graded interphase*

The sinusoidal pulse considered in this study is a rectified sine wave, hereafter referred to as sinusoidal, such that the interphase modulus is always positive. The sinusoidal variation of the interphase modulus is given by

$$E_2 = E_{\min} + (E_{\max} - E_{\min}) \left| \sin\left(\frac{n\pi x}{L}\right) \right|, \tag{15}$$

where $E_{\min}$ denotes the minimum value of the interphase modulus and n represents the total number of peaks. Variation of the interphase modulus according to single, two and four sinusoidal pulses is shown in Figs. 2(d), 3(a) and 3(b), respectively. A definite peak value of the interphase modulus can be identified in sinusoidal variation. Furthermore, the variation from the minimum to maximum modulus is noticed be smooth, see Figs. 2(c) and 2(d).

2.2.3. *Triangular pulse graded interphase*

Distribution of the interphase modulus according to a triangular pulse can be estimated by

$$E_2 = E_{\min} + (E_{\max} - E_{\min}) \left(\frac{2}{\pi}\right) \left| \sin^{-1}\left[\sin\left(\frac{n\pi x}{L}\right)\right] \right|. \tag{16}$$

Variation of the interphase modulus according to single, two and four triangular pulses is shown in Figs. 2(d), 3(a) and 3(b), respectively. In triangular pulse, the variation from minimum to maximum modulus is linear, see Fig. 2(d). Therefore, the point of intersection of the minimum–maximum and maximum–minimum lines indicates the peak interphase modulus. As a result, a sharp peak value of the interphase modulus can be identified in triangular variation.

An estimation of Eqs. (12) and (13) considering modulus grading according to single sinusoidal pulse, see Eq. (15), using MAPLE is provided in Eqs. (B.1) and (B.4), respectively. Concerned equations considering modulus grading according to square and triangular pulses are observed to be complex and hence omitted here for brevity.

3. Results and Discussion

In this section, the influence of domain length, grading profile, tablet and interphase thickness on the interfacial stresses, apart from the variation of the peel stress is studied. The parameters adopted in the simulations are listed in Table 2. A uniaxial load equal to 100 MPa is specified to the upper tablet parallel to its length. The lower tablet is fixed.

Table 2. Material properties of the tablets and the interphase of a single lap joint shown in Fig. 1. The properties are adopted from [Barthelat and Espinosa (2007); Jackson *et al.* (1988); Espinosa *et al.* (2009); Ni *et al.* (2015)].

Constituent	Young's modulus (GPa)	Poisson's ratio	Length (μm)	Thickness (μm)
tablets	100	0.3	8	0.4
interphase	2.8	0.4	8	0.025

3.1. *Influence of domain length*

The applied load is transferred through shear in single lap joints. Therefore, sufficient domain length is required to ensure complete load transfer [Nairn (1997, 2001, 2004)]. In order to investigate the influence of domain length, simulations are performed considering domain lengths equal to 4 μm, 8 μm and 12 μm. Distribution of the interfacial shear stresses employing ungraded, and single pulse; square, sinusoidal and triangular elastic moduli-graded interphases, along with the peak interfacial shear stresses is plotted in Fig. 4.

Variation of the interfacial shear stresses adopting variation of interphase elastic modulus according to ungraded, single pulse square, sinusoidal and triangular with a domain length of 4 μm is plotted in Fig. 4(a). According to Fig. 4(a), the peak stresses in ungraded and square pulse modulus graded interphases are observed to be close, indicating that the grading according to square pulse has not significantly improved the load transfer mechanics. This is because of the abrupt changes in elastic modulus for every one third length of the domain, see Figs. 2(b) and 2(d), leading to lower effective modulus as compared to modulus grading based on sinusoidal and triangular pulses, see Table 1. On the other hand, the peak stresses are estimated to reduce by 11.67% when the interphase modulus is graded according to sinusoidal/triangular laws. This can be attributed to wide distribution of the elastic modulus along the domain length and higher effective modulus.

The studies are extended to domain lengths of 8 μm and 12 μm. Variation of the interfacial shear stresses considering a domain length of 8 μm is shown in Fig. 4(b). Comparison of interfacial shear stresses with ungraded and graded interphases, considering domain lengths of 4 μm and 8 μm and 8 μm and 12 μm is shown in Figs. 4(c) and 4(d), respectively. Distribution of the peak shear stresses as a function of domain length is shown in Fig. 4(e). According to Fig. 4(e), the peak shear stresses are observed to drop by $\approx$30% when the domain length changes from 4 μm to 8 μm. Furthermore, the minimum stresses are found to be $\approx$50% of the peak stresses when the domain length is equal to 8 μm. Whereas, the variation is more flatter when the domain length is equal to 4 μm, see Fig. 4(a). This means the stresses are maximum for most part of the domain, which can lead to quicker delamination. Therefore, minimum required length of the domain for complete shear transfer for the considered single lap joint is more than 4 μm. According to Figs. 4(d) and 4(e), the drop in peak stresses for a domain length of 12 μm, as compared to the domain

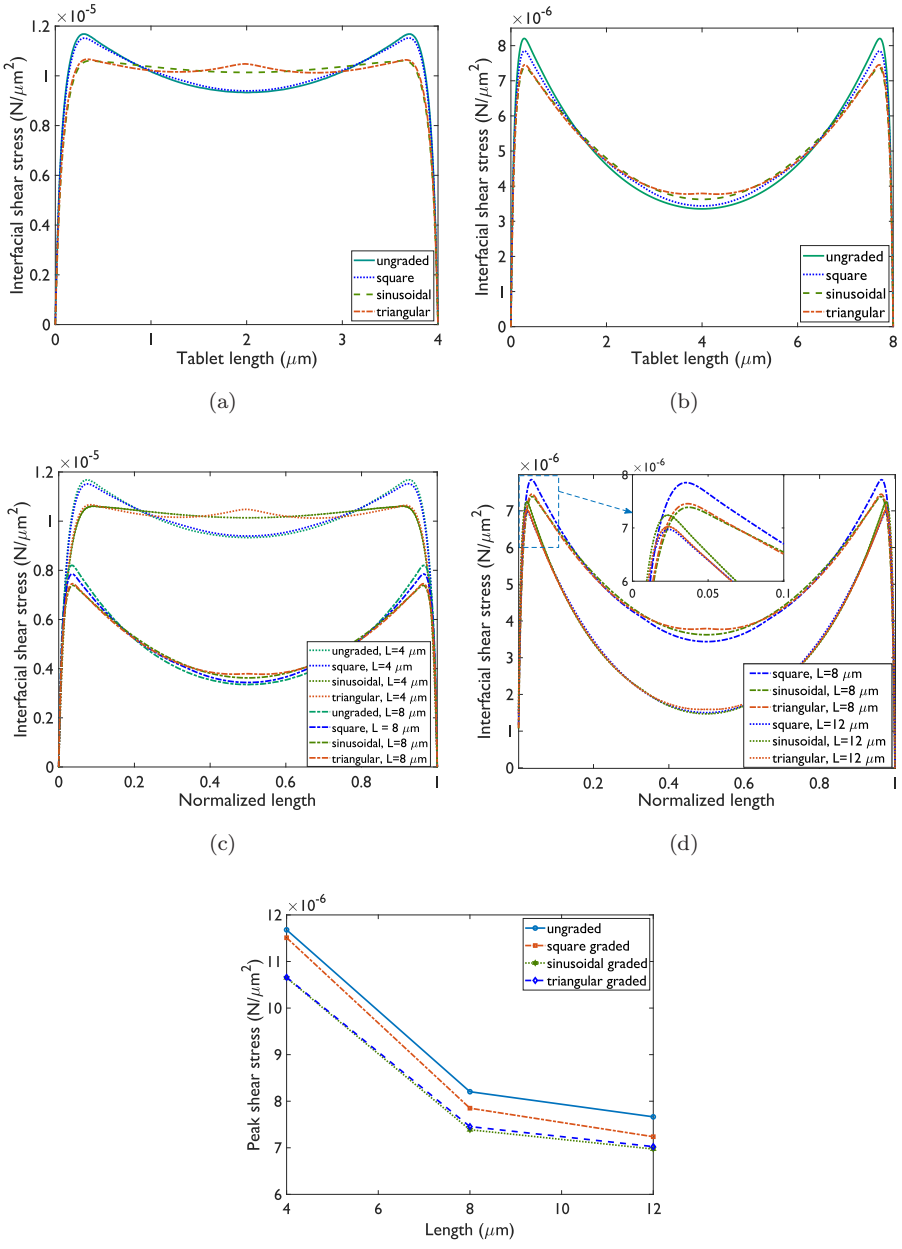

Fig. 4. Distribution of the interfacial shear stresses considering ungraded, and square, sinusoidal and triangular pulse graded elastic moduli interphases, with domain lengths equal to (a) 4 μm and (a) 8 μm. Comparison of interfacial shear stresses with ungraded and graded interphases, considering domain lengths of (c) 4 μm and 8 μm and (d) 8 μm and 12 μm. (e) Distribution of the peak shear stresses as a function of domain length. Single pulses are used in all the simulations with graded interphase.

length of 8 μm, is estimated to be less than 10%, which is not significant as compared to the drop when the domain length changes from 4 μm to 8 μm. Moreover, the minimum stresses are ≈13% of the peak stresses for the domain length of 12 μm, see Fig. 4(d). Such shallow distribution results in concentration of stresses and hence, leads to damage initiation around the edges. Hence, a domain length of 8 μm is used in the all the simulations.

3.2. *Influence of modulus grading profile*

In order to study the influence of modulus grading profile on the shear stress distribution, the elastic modulus of the interphase is modified considering two, three and

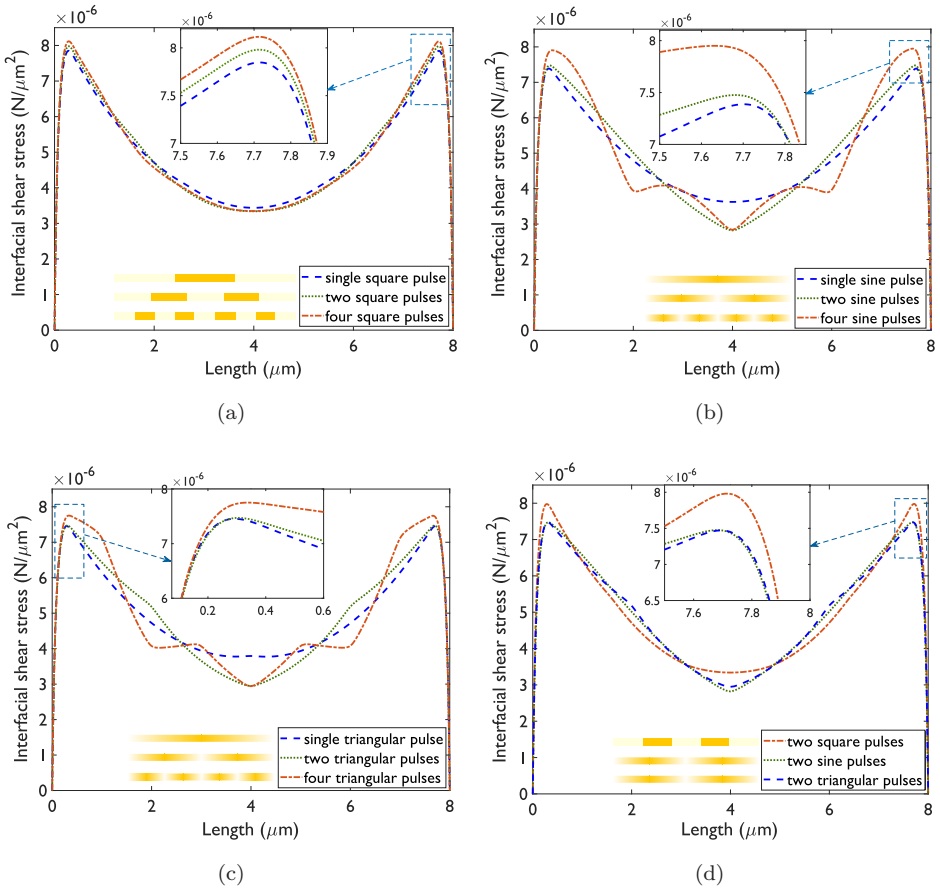

Fig. 5. Distribution of the interfacial shear stresses considering single, two and four pulse graded elastic moduli interphases, with domain lengths equal to 8 μm and (a) square, (b) sinusoidal and (c) triangular laws. A comparison of the interfacial shear stresses with square, sinusoidal and triangular graded interphases, considering (d) two and (e) four pulses. (f) Distribution of the peak shear stresses as a function of number of pulses.

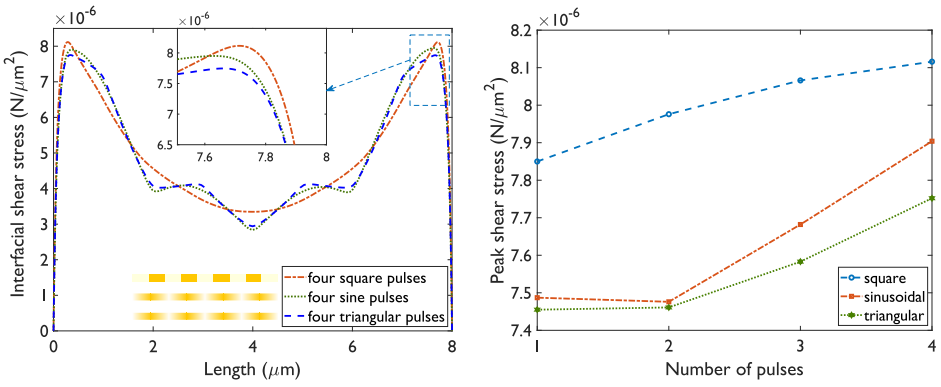

(e) (f)

Fig. 5. (*Continued*)

four pulses of square, sinusoidal and triangular profiles, see Figs. 3 and 5. Distribution of the interfacial shear stresses considering the domain length equal to 8 μm and single, two and four pulse-graded elastic moduli interphases, according to square, sinusoidal and triangular laws is shown in Figs. 5(a), 5(b) and 5(c), respectively. Furthermore, a comparison of the interfacial shear stresses with square, sinusoidal and triangular graded interphases, considering two and four pulses is provided in Figs. 5(d) and 5(e), respectively. Whereas, the peak shear stresses as a function of number of pulses are indicated in Fig. 5(f).

According to Fig. 5(a), the peak stresses are observed to slightly increase with the increase in number of square pulses. The effective modulus gradually increases with increase in number of square pulses, see Table 1. Therefore, as shown in Fig. 5(f), the peak shear stresses continue to raise with increase in number of square pulses. On the other hand, the peak stresses are almost same for single and two sinusoidal and triangular pulses, see Figs. 5(b) and 5(c). Whereas, the peak stresses are observed to raise with four sinusoidal and triangular pulses, as compared to the single and two pulses. Although the effective modulus of the sinusoidal and triangular pulses does not vary with the number of pulses, the distribution of the elastic modulus of the interphase with increased number of pulses (see Fig. 3) alters the stress profile. However, the peak stresses when the moduli is graded according to sinusoidal and triangular laws are estimated to be $\approx$4.4% lower with respect to the corresponding square grading, see Fig. 5(f).

According to Figs. 5(d) and 5(e), the peak shear stresses are maximum when the modulus is graded according to square pulse. This is mainly due to lower effective interphase modulus of the square pulse, as compared to sinusoidal and triangular pulses, see Table 1. Furthermore, the effective modulus of the ungraded interphase is less than that of square pulse graded interphase. As a result, the peak stresses are highest in case of ungraded modulus interphase, as shown in Fig. 4(e). Similar trend is observed with graded interphases as well, where the peak stresses are

higher in square modulus-graded interphase as compared to sinusoidal and triangular graded interphases. Therefore, with increased number of pulses, the peak shear stresses are found to be increasing. As a result, selective grading of the interphase is recommended to arrive at the required distribution of the interfacial stresses.

3.3. *Influence of tablet thickness*

The tablet thickness plays a crucial role in controlling the peak interfacial shear stresses. Therefore, variation of interfacial shear stresses considering a domain length of 8 μm is studied for tablet thicknesses of 0.2 μm, 0.4 μm, 0.6 μm and 0.8 μm, with square, sinusoidal and triangular pulses. A comparison of the interfacial shear stresses considering modulus variation according to single pulse square

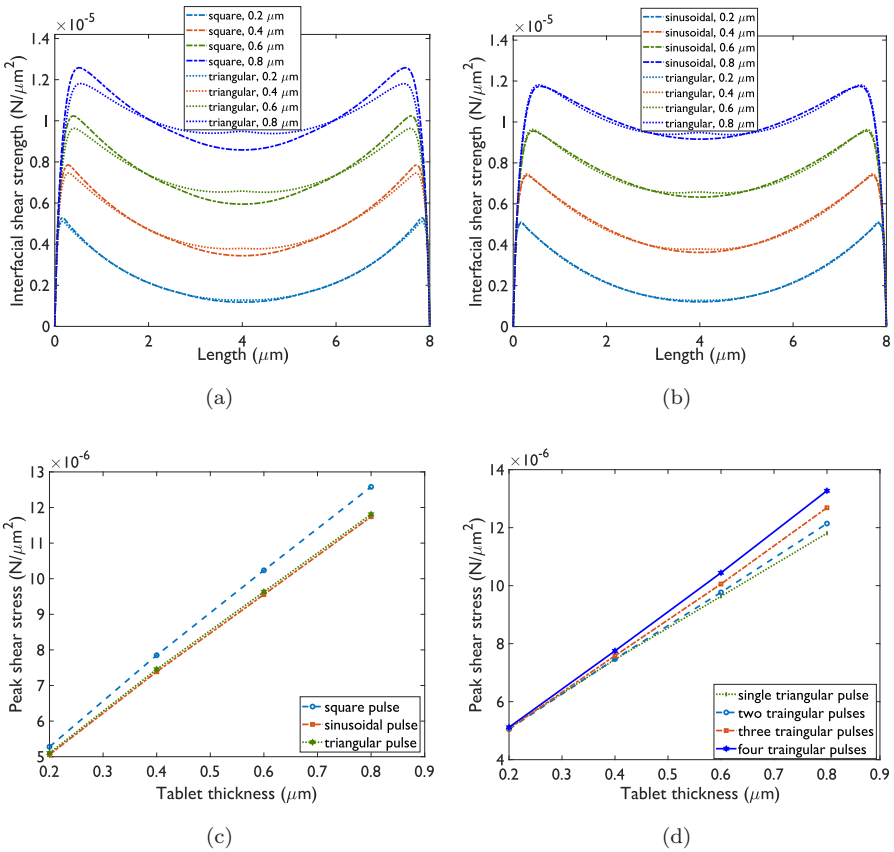

Fig. 6. Comparison of the interfacial shear stresses considering elastic modulus of the interphase according to single pulse (a) square and triangular laws and (b) sinusoidal and triangular laws, for tablet thickness varying from 0.2 μm to 0.8 μm. Variation of the peak interfacial stresses as a function of tablet thickness considering (c) square, sinusoidal and triangular pulses and (d) single, two, three and four triangular pulses.

and triangular laws and sinusoidal and triangular laws, for tablet thickness varying from 0.2 μm to 0.8 μm is shown in Figs. 6(a) and 6(b), respectively. Whereas, Figs. 6(c) and 6(d) represent the variation of the peak interfacial stresses as a function of tablet thickness considering square, sinusoidal and triangular pulses and single, two, three and four triangular pulses, respectively.

According to Figs. 6(a) and 6(b), the peak stresses continue to increase with increase in tablet thickness. Furthermore, as discussed in the previous section, the peak stresses with square pulses are always on the higher side as compared to the sinusoidal pulses, see Fig. 6(c). Furthermore, the increase in number of pulses also increases the peak stresses with increased tablet thickness, as shown in Fig. 6(d). Therefore, the increase in tablet thickness leads to an increase in frictional resistance, resulting in increased peak stresses.

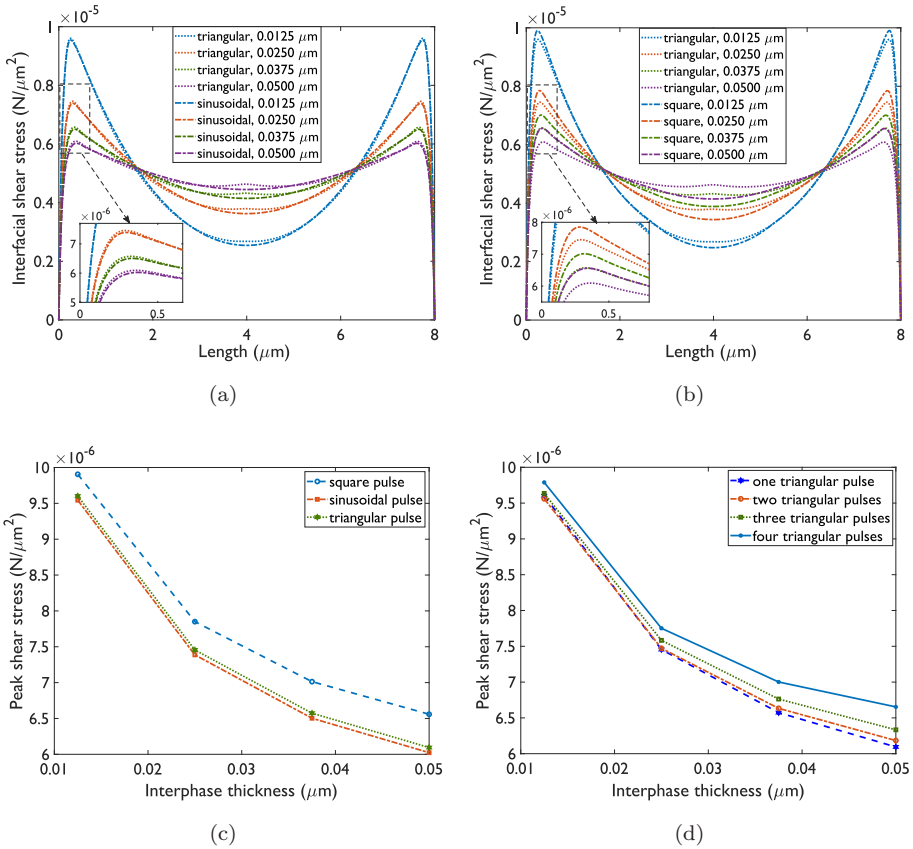

Fig. 7. Comparison of the interfacial shear stresses by varying the elastic modulus of the interphase according to single pulse (a) triangular and sinusoidal laws and (b) triangular and square laws, for interphase thickness varying from 0.0125 μm to 0.05 μm. Variation of the peak interfacial stresses as a function of interphase thickness considering (c) square, sinusoidal and triangular pulses and (d) single, two, three and four triangular pulses.

3.4. *Influence of interface thickness*

The thickness of the interphase is critical in smooth shear transfer of the applied loads. Therefore, simulations are performed with varying interphase thickness considering a domain length of 8 μm and tablet thickness of 0.4 μm. Comparison of the interfacial shear stresses by varying the elastic modulus of the interphase according to single pulse triangular and sinusoidal laws and triangular and square laws, for interphase thickness varying from 0.0125 μm to 0.05 μm is plotted in Figs. 7(a) and 7(b), respectively. Moreover, variation of the peak interfacial stresses as a function of interphase thickness considering square, sinusoidal and triangular pulses and single, two, three and four triangular pulses is shown in Figs. 7(c) and 7(d), respectively.

Based on Fig. 7(a), the peak stresses are observed to increase with decrease in interphase thickness. Therefore, the peak stresses are maximum for an interphase thickness of 0.0125 μm. Also, the minimum stresses are estimated to be 30% of the maximum stresses, resulting in a steep variation of the interfacial shear stresses towards the center of the domain. Such steep gradients result in quicker damage initiation and hence are not recommended for lap joints. On the other hand, the peak stresses are observed to reduce by $\approx$20% when the interphase thickness is increased to 0.025 μm, see Fig. 7(c). Further reduction in peak stresses with increase in interphase thickness is noticed to be marginal, see Fig. 7. According to Fig. 7(d), the peak stresses are found to be increasing with increase in number of pulses, in particular, at higher interphase thickness. Therefore, an interphase thickness of 0.025 μm is adopted in the present simulations.

3.5. *Peel stresses*

The peel stresses estimated using Eq. (2) are plotted in Fig. 8. Comparison of the peel stresses by varying the elastic modulus of the interphase according to single pulse; square, sinusoidal and triangular laws, apart from an ungraded interphase and four square, sinusoidal and triangular pulses, considering a domain length of 8 μm, is plotted in Figs. 8(a) and 8(b), respectively. A close-up of the peak stresses is provided in the inset pictures.

The peel stresses are observed to follow similar trend irrespective of the type of grading, including ungraded interphases. Therefore, according to Fig. 8, the peak stresses (see the insets of Figs. 8(a) and 8(b)) are observed to be close, where they are maximum with square-graded interphase and minimum with triangular-graded interphase.

4. Physics Informed Neural Networks

The operation of artificial neural networks (ANN) is similar to the function of biological (human) neural networks. The information flows only in the forward direction in feed forward neural network (FNN), without any loops, through the input nodes to the output nodes. FNNs are mainly employed for supervised learning

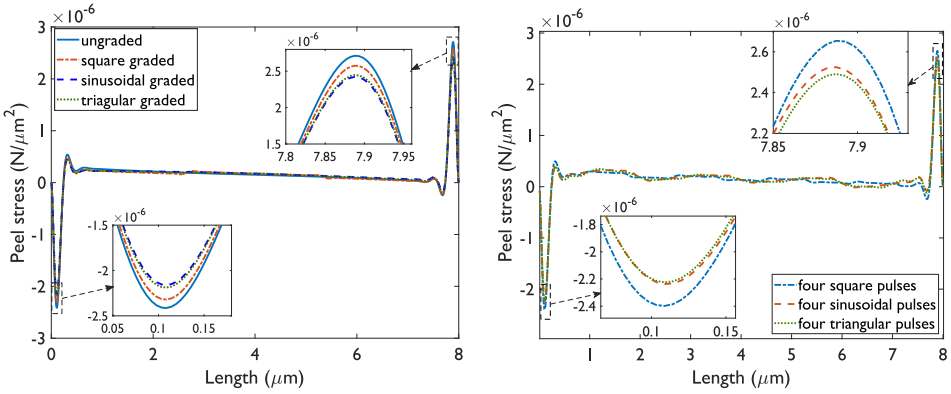

(a) (b)

Fig. 8. Comparison of the peel stresses by varying the elastic modulus of the interphase according to single pulse (a) square, sinusoidal and triangular laws, apart from an ungraded interphase and (b) four square, sinusoidal and triangular pulses, considering a domain length of 8 μm.

neither sequential nor time-dependent data. In general, an artificial neural network consists of an input layer, possibly few hidden layers, and an output layer, see Fig. 9. However, in case of single-layer artificial neural network, the hidden layers do not exist. Hence, an m-layer ANN on an n-dimensional input $\mathbf{x} = \{x_1, x_2, \ldots, x_n\}$, computes a one-dimensional output OP.

Figure 9 shows a schematic of a physics informed feed forward neural network to solve partial differential equations, for the given initial and boundary conditions. As shown in Fig. 9, an estimation of the stresses σ_1 and σ_3 is performed using the dimensions and material properties of the constituents of a lap joint. Furthermore, automatic differentiation (AD) is employed to estimate the derivatives of the stresses σ_1 and σ_3, which are further used in the calculation of the loss function. The loss

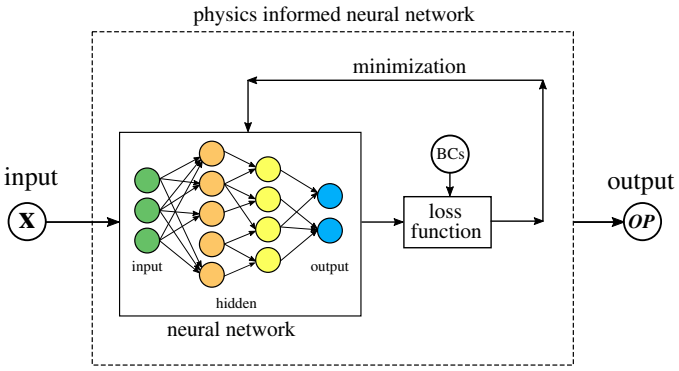

Fig. 9. Schematic of a physics informed neural network to solve partial differential equations considering boundary and initial conditions.

function is minimized through an iterative process to arrive at the final values of the axial stresses σ_1 and σ_3 in Tables 1 and 2, respectively, such that the boundary conditions are satisfied.

The implemented aspects of the proposed neural network using TensorFlow framework are adopted from Sharma *et al.* (2021). The developed neural network is trained using google Colab. The least value of the loss function is arrived by following an iterative process, thus, fixing the architecture of the neural network. A fully connected feed forward artificial neural network architecture with three hidden layers, where each layer contains 500 neurones, one input layer and one output layer containing two output neurons, is selected for the analysis. The strength of the connections that connect the neurons can be changed through the learning process. A numeric value is assigned to each neuron, known as weight. The output of each neuron can be written as

$$y = f\left(b + \sum_{i=1}^{n} \mathbf{x}^{(i)} w_i\right), \tag{17}$$

where f denotes the activation function, n is the number of inputs to the neuron, w represents the weight of the connection, $\mathbf{x}$ is the input, and the activation function is offset by the bias b. The hyperbolic tangent function is used as activation function here. Xavier initialization function is employed here for the initialization of the weights and biases. Xavier initialization controls the constant variance across every layer, with the output centered around 0, indicating that the mean is 0. The network is thoroughly tested for the convergence and repeatability of the results, until the developed network is observed to be producing stable results every time. A combination of L-BFGS-B and Adam optimizer is adopted to optimize the loss function. When the loss function is close to zero, the solution can be identified to be converging.

The developed PINN model is trained for 200 iterations, and the cost as a function of iterations is shown in Fig. 10(a). A drastic drop in the cost function in first 40 iterations is evident, indicating that a better local minimum can be found after 40 iterations. However, the error tolerance for the cost function is prescribed as 10^{-12} machine accuracy. This means, after 200 iterations, the network will switch to Adam optimizer until reaching the prescribed machine accuracy. A maximum of 50000 iterations are prescribed under any circumstances.

The governing equations (B.1) and (B.4) arrived from MAPLE are specified to the PINN as equations to be solved. The loads and boundary conditions mentioned in Sec. 3 are extended to the neural network model. A comparison of the interfacial shear stresses estimated using the analytical and PINN models, considering a single pulse sinusoidal graded interphase modulus is shown in Fig. 10(b). A close agreement of the results is evident in Fig. 10(b). However, in reality, the peak stresses occur slightly inside the domain, which are reproduced in the analytical results, see Fig. 10(b). Whereas, the peak stresses estimated from the PINN model are found to be exactly lying on the edges. Therefore, the load transfer mechanics

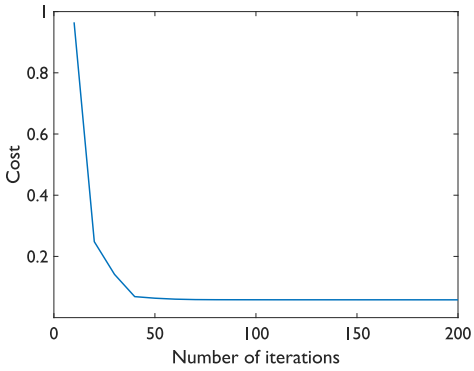

(a)

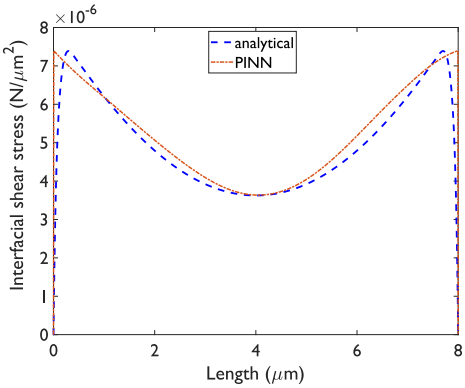

(b)

Fig. 10. (a) Variation of the cost function as a function of number of iterations. (b) Comparison of interfacial shear stress estimated from the developed analytical and PINN models.

are not exactly reproduced in the PINN solution. This issue is also reflected in the numerical results, see Fig. C.1.

5. Conclusions

The mechanics of a single lap joint are altered by profiling the interphase modulus according to square, sinusoidal and triangular pulse laws. A uniaxial loading parallel to the tablet length is applied on the right edge of the upper tablet while keeping the lower tablet fixed. Closed form solutions are obtained by solving the governing differential equations using MAPLE software. The interfacial shear stresses estimated using the proposed method are compared to the results from a numerical analysis and both results are in close agreement. Change in peak interfacial stresses with different elastic modulus profiles is investigated. Furthermore, the studies are

extended considering variation of the interphase modulus according to single, two, three and four pulse square, sinusoidal and triangular laws.

A deep machine learning-based physics informed neural network model is developed to estimate the interfacial shear stresses with varying interphase modulus. The results obtained through the DML-based approach are then compared with the exact solution obtained using MAPLE software. The peak interfacial shear stresses are observed to decrease according to the square, sinusoidal and triangular laws. On the other hand, the increase in number of pulses is found to increase the peak stresses.

An analytical framework is proposed here to estimate the interfacial shear stresses considering modulus graded interphases according to square, sinusoidal and triangular pulses. Furthermore, a deep learning approach to solve the complex differential equations associated with engineered interphases in a single lap joint is also developed. The correct hyper-parameters for the neural network model are obtained through an iterative method. Although the training of the neural network requires computationally expensive approaches, we believe that the proposed method will be useful in providing a quick solution to a variety of practical problems in future.

Acknowledgments

PRB is thankful to the Science and Engineering Research Board (SERB), Department of Science and Technology (DST), India, for funding this research through Grant number SRG/2019/001581.

Appendix A. Analytical Expressions

A.1. *Boundary conditions*

The boundary conditions of the proposed single lap joint are given by

At $x = 0$:

$$\sigma_x^{(3)} = \rho\sigma_0, \quad \sigma_x^{(2)} = 0, \quad \sigma_x^{(1)} = 0, \tag{A.1a}$$

$$\tau_{xy}^{(3)} = 0, \quad \tau_{xy}^{(2)} = 0, \quad \tau_{xy}^{(1)} = 0. \tag{A.1b}$$

At $x = L$:

$$\sigma_x^{(1)} = \sigma_0, \quad \tau_{xy}^{(1)} = 0, \tag{A.1c}$$

At $y = c$:

$$\tau_{xy}^{(2)}(y = c) = \tau_{xy}^{(1)}(y = c). \tag{A.1d}$$

A.2. *Force equilibrium*

Considering the force equilibrium

$$\sigma_1 h_1 + \sigma_2 h + \sigma_3 h_2 = \sigma_0 h_1, \tag{A.2a}$$

$$\sigma_2 = \alpha_1(\sigma_0 - \sigma_1) - \alpha_2\sigma_3, \tag{A.2b}$$

$$\sigma_2' = -\alpha_1\sigma_1' - \alpha_2\sigma_3', \tag{A.2c}$$

$$\sigma_2'' = -\alpha_1\sigma_1'' - \alpha_2\sigma_3'', \tag{A.2d}$$

$$\sigma_2''' = -\alpha_1\sigma_1''' - \alpha_2\sigma_3''', \tag{A.2e}$$

$$\sigma_2'''' = -\alpha_1\sigma_1'''' - \alpha_2\sigma_3'''', \tag{A.2f}$$

where $\alpha_1 = \frac{h_1}{h}$ and $\alpha_2 = \frac{h_2}{h}$.

A.3. *Coefficients*

The coefficients of the energy functional Ψ are given by

$$A_1 = \left(\frac{h_1^5}{40E_1} + \frac{h_1^2(4h^3 + 3hh_1^2 + 6h_1h^2)}{24E_2} + \frac{b(2h_1h + h_1^2)^2}{8E_3}\right), \tag{A.3a}$$

$$A_2 = \left(\frac{h^5}{40E_2} + \frac{bh^4}{8E_3}\right), \tag{A.3b}$$

$$A_3 = \frac{b^5}{15E_3}, \tag{A.3c}$$

$$A_4 = \left(\frac{h_1(4ch^3 - c^4 + 3b^4 + 6c^2b^2 - 8cb^3)}{24E_2} + \frac{bh^2(2h_1h + h_1^2)}{4E_3}\right), \tag{A.3d}$$

$$A_5 = -\frac{b^3h^2}{6E_3}, \tag{A.3e}$$

$$A_6 = -\frac{b^3(2h_1h + h_1^2)}{6E_3}, \tag{A.3f}$$

$$A_7 = \frac{\nu_1 h_1^3}{6E_1}, \tag{A.3g}$$

$$A_8 = -\frac{\nu_2 h^3}{6E_2}, \tag{A.3h}$$

$$A_9 = -\frac{\nu_2 h_1(2ch - c^2 + b^2 + hh_1)}{2E_2}, \tag{A.3i}$$

$$A_{10} = -\frac{\nu_3 bh^2}{2E_3}, \tag{A.3j}$$

$$A_{11} = -\frac{\nu_3 b(2h_1 h + h_1^2)}{2E_3}, \tag{A.3k}$$

$$A_{12} = \frac{2\nu_3 b^3}{6E_3}, \tag{A.3l}$$

$$A_{13} = \left(\frac{(1+\nu_1)h_1^3}{6E_1} + \frac{(1+\nu_2)hh_1^2}{2E_2}\right), \tag{A.3m}$$

$$A_{14} = \frac{(1+\nu_2)h^3}{6E_2}, \tag{A.3n}$$

$$A_{15} = \frac{(1+\nu_3)b^3}{6E_3}, \tag{A.3o}$$

$$A_{16} = \frac{(1+\nu_2)h^2 h_1}{2E_2}, \tag{A.3p}$$

$$A_{17} = \frac{h_1}{2E_1}, \tag{A.3q}$$

$$A_{18} = \frac{h}{2E_2}, \tag{A.3r}$$

$$A_{19} = \frac{b}{2E_3}. \tag{A.3s}$$

$$B_1 = 2(A_1 + \alpha_1^2 A_2 - \alpha_1 A_4), \tag{A.4a}$$

$$B_2 = (2\alpha_1\alpha_2 A_2 - \alpha_2 A_4 - \alpha_1 A_5 + A_6), \tag{A.4b}$$

$$B_3 = (A_7 + \alpha_1^2 A_8 - \alpha_1 A_9 + (2A_{13} + 2\alpha_1^2 A_{14} - 2\alpha_1 A_{16}) - (A_7 + \alpha_1^2 A_8 - \alpha_1 A_9)), \tag{A.4c}$$

$$B_4 = ((\alpha_1\alpha_2 A_8 - \alpha_2 A_9 - \alpha_1 A_{10} + A_{11}) + (2\alpha_1\alpha_2 A_{14} - \alpha_2 A_{16}) - \alpha_1\alpha_2 A_8), \tag{A.4d}$$

$$B_5 = -2(A_{17} + \alpha_1^2 A_{18}), \tag{A.4e}$$

$$B_6 = -2\alpha_1\alpha_2 A_{18}, \tag{A.4f}$$

$$B_7 = -2\alpha_1^2 A_{18}. \tag{A.4g}$$

$$C_1 = (2\alpha_1\alpha_2 A_2 - \alpha_2 A_4 - \alpha_1 A_5 + A_6), \tag{A.5a}$$

$$C_2 = 2(\alpha_2^2 A_2 + A_3 - \alpha_2 A_5), \tag{A.5b}$$

$$C_3 = (\alpha_1\alpha_2 A_8 + (2\alpha_1\alpha_2 A_{14} - \alpha_2 A_{16}) - (\alpha_1\alpha_2 A_8 - \alpha_2 A_9 - \alpha_1 A_{10} + A_{11})), \tag{A.5c}$$

$$C_4 = ((\alpha_2^2 A_8 - \alpha_2 A_{10} + A_{12}) + 2(\alpha_2^2 A_{14} + A_{15}) - (\alpha_2^2 A_8 - \alpha_2 A_{10} + A_{12})), \tag{A.5d}$$

$$C_5 = -2\alpha_1\alpha_2 A_{18}, \tag{A.5e}$$

$$C_6 = -2(\alpha_2^2 A_{18} + A_{19}), \tag{A.5f}$$

$$C_7 = -2\alpha_1\alpha_2 A_{18}\sigma_0. \tag{A.5g}$$

Appendix B. Governing Differential Equations

In this section, Eqs. (12) and (13) are estimated considering single sinusoidal pulse, see Eq. (15), using MAPLE. Therefore, ODE_1 (Eq. (12)) can be written as

$$\mathrm{ODE}_1 = \frac{N_1}{D_1}, \tag{B.1}$$

where N_1 is given by

$$\begin{aligned} N_1 = {} & [(1.901714285 \times 10^{-12})\cos(0.3926990817x)^6 + (-4.204712907 \times 10^{-10} \\ & \times \sin(0.3926990817x) - 6.05564448 \times 10^{-9})\cos(0.3926990817x)^4 \\ & + (3.662552137 \times 10^{-8}\sin(0.3926990817x) + 1.186867342 \times 10^{-7}) \\ & \times \cos(0.3926990817x)^2 - 1.953836008 \times 10^{-7}\sin(0.3926990817x) \\ & - 2.078650043 \times 10^{-7}]\sigma_1'''' + [(-9.570312496 \times 10^{-11}\sin(0.3926990817x) \\ & - 1.435307716 \times 10^{-9})\cos(0.3926990817x)^4 + (8.802574932 \times 10^{-9} \\ & \times \sin(0.3926990817x) + 2.870436063 \times 10^{-8})\cos(0.3926990817x)^2 \\ & - 4.746125635 \times 10^{-8}\sin(0.3926990817x) - 5.052598849 \times 10^{-8}] \\ & \times \sigma_3'''' + [(3.030931122 \times 10^{-10})\cos(0.3926990817x)^5 \\ & + (-3.637436223 \times 10^{-9}\sin(0.3926990817x) - 1.697608417 \times 10^{-8}) \\ & \times \cos(0.3926990817x)^3 + (3.638010202 \times 10^{-8}\sin(0.3926990817x) \\ & + 4.123214283 \times 10^{-8})\cos(0.3926990817x)]\sigma_1''' + [(7.525510202 \times 10^{-11}) \\ & \times \cos(0.3926990817x)^5 + (-9.03499681 \times 10^{-10}\sin(0.3926990817x) \\ & - 4.218231822 \times 10^{-9})\cos(0.3926990817x)^3 + (9.042889028 \times 10^{-9} \\ & \times \sin(0.3926990817x) + 1.025047831 \times 10^{-8})\cos(0.3926990817x)] \\ & \times \sigma_3''' + [(-2.603537415 \times 10^{-10})\cos(0.3926990817x)^6 + (-1.019208132 \end{aligned}$$

$$\times 10^{-7}\sin(0.3926990817x) - 1.563714057 \times 10^{-6})\cos(0.3926990817x)^4$$
$$+ (9.663367471 \times 10^{-6}\sin(0.3926990817x) + 0.00003161615909)$$
$$\times \cos(0.3926990817x)^2 - 0.00005238987302\sin(0.3926990817x)$$
$$- 0.00005578559962]\sigma_1'' + [(-1.028423681 \times 10^{-7})\sin(0.3926990817x)$$
$$- 1.542768476 \times 10^{-6})\cos(0.3926990817x)^4 + (9.462855862^{\times}10^{-6}$$
$$\times \sin(0.3926990817x) + 0.00003085802864)\cos(0.3926990817x)^2$$
$$- 0.00005101914627\sin(0.3926990817x) - 0.00005431033693]$$
$$\times \sigma_3'' + 1.485714285 \times 10^{-9}\sigma_1\cos(0.3926990817x)^6 + (4.188790055 \times 10^{-8}\sigma_1'$$
$$+ 5.310787432 \times 10^{-8}\sigma_3')\cos(0.3926990817x)^5 + ((-0.00002744562093\sigma_1$$
$$- 0.00002741887806\sigma_3 + 0.00002741887806)\sin(0.3926990817x)$$
$$- 0.0004113704112\sigma_3 - 0.0004115754397\sigma_1 + 0.0004113704112)$$
$$\times \cos(0.3926990817x)^4 + ((-5.026548064 \times 10^{-7}\sigma_1' - 6.37294491710^{-7}\sigma_3')$$
$$\times \sin(0.3926990817x) - 2.34572243 \times 10^{-6}\sigma_1' - 2.974040961 \times 10^{-6}\sigma_3')$$
$$\times \cos(0.3926990817x)^3 + ((0.002524284343\sigma_1 + 0.002523428571\sigma_3$$
$$- 0.002523428571)\sin(0.3926990817x) + 0.008231363769\sigma_1$$
$$+ 0.008229153026\sigma_3 - 0.008229153026))\cos(0.3926990817x)^2$$
$$+ ((5.026548066 \times 10^{-6}\sigma_1' + 6.372944918 \times 10^{-6}\sigma_3')\sin(0.3926990817x)$$
$$+ 5.696754474 \times 10^{-6}\sigma_1' + 7.222670908 \times 10^{-6}\sigma_3')\cos(0.3926990817x)$$
$$+ (0.01360588972 - 0.01360888492\sigma_1 - 0.01360588972\sigma_3)$$
$$\times \sin(0.3926990817x) - 0.0144865392\sigma_1 - 0.01448344891\sigma_3$$
$$+ 0.01448344891) \tag{B.2}$$

and D_1 is given by

$$\begin{aligned} D_1 = {} & (0.02040816326\cos(0.3926990817x)^6 + (-2.81632653 \\ & - 0.3673469388\sin(0.3926990817x))\cos(0.3926990817x)^4 \\ & + (30.36734693 + 11.75510204\sin(0.3926990817x)) \\ & \times \cos(0.3926990817x)^2 - 42.44897958 - 41.14285714 \\ & \times \sin(0.3926990817x)). \end{aligned} \tag{B.3}$$

In the similar lines, N_2 is given by

$$\text{ODE}_2 = \frac{N_2}{D_2}. \tag{B.4}$$

where N_2 is given by:

$$\begin{aligned}
N_2 = {} & [(1.901714285 \times 10^{-12}) \cos(0.3926990817x)^6 + (-1.713880637 \times 10^{-10} \\
& \times \sin(0.3926990817x) - 2.31995411 \times 10^{-9}) \cos(0.3926990817x)^4 \\
& + (1.371532525 \times 10^{-8} \sin(0.3926990817x) + 4.398189531 \times 10^{-8}) \\
& \times \cos(0.3926990817x)^2 - 7.187068635 \times 10^{-8} \sin(0.3926990817x) \\
& - 7.638047004 \times 10^{-8}]\sigma_3'''' + [(-9.562340562 \times 10^{-11} \sin(0.3926990817x) \\
& - 1.434988839 \times 10^{-9}) \cos(0.3926990817x)^4 + (8.803451849 \times 10^{-9} \\
& \times \sin(0.3926990817x) + 2.870874521 \times 10^{-8}) \cos(0.3926990817x)^2 \\
& - 4.746221301 \times 10^{-8} \sin(0.3926990817x) - 5.051992984 \times 10^{-8}] \\
& \times \sigma_1'''' + [(7.521524234 \times 10^{-11}) \cos(0.3926990817x)^5 + (-9.023836094 \\
& \times 10^{-10} \sin(0.3926990817x) - 4.210259884 \times 10^{-9}) \cos(0.3926990817x)^3 \\
& + (9.020248722 \times 10^{-9} \sin(0.3926990817x) + 1.022209821 \times 10^{-8}) \\
& \times \cos(0.3926990817x)]\sigma_1''' + [(1.077407525 \times 10^{-10}) \\
& \times \cos(0.3926990817x)^5 + (-1.29288903 \times 10^{-9} \sin(0.3926990817x) \\
& - 6.033482141 \times 10^{-9}) \cos(0.3926990817x)^3 + (1.292889031 \times 10^{-8} \\
& \times \sin(0.3926990817x) + 1.465274234 \times 10^{-8}) \cos(0.3926990817x)] \\
& \times \sigma_3''' + [(-2.603537415 \times 10^{-10}) \cos(0.3926990817x)^6 \\
& + (-3.719723695 \times 10^{-8} \sin(0.3926990817x) - 5.92515582 \times 10^{-7}) \\
& \times \cos(0.3926990817x)^4 + (3.705272777 \times 10^{-6} \sin(0.3926990817x) \\
& + 0.00001218529141) \cos(0.3926990817x)^2 - 0.00002026276688 \\
& \times \sin(0.3926990817x) - 0.0000215867138]\sigma_3'' \\
& + [(-1.028423681 \times 10^{-7}) \sin(0.3926990817x) - 1.542768487 \times 10^{-6}) \\
& \times \cos(0.3926990817x)^4 + (9.462855888^{\times}10^{-6} \sin(0.3926990817x) \\
& + 0.00003085802721) \cos(0.3926990817x)^2 - 0.0000510191399
\end{aligned}$$

$$\times \sin(0.3926990817x) - 0.00005431034402]\sigma_1'' + 1.485714285 \times 10^{-9}\sigma_1$$
$$\times \cos(0.3926990817x)^6 + (2.767594449 \times 10^{-8}\sigma_1' + 1.645597071 \times 10^{-8}\sigma_3')$$
$$\times \cos(0.3926990817x)^5 + ((-0.00002742387161\sigma_1 - 0.00002745061448\sigma_3$$
$$+ 0.00002742387161)\sin(0.3926990817x) - 0.0004116054009\sigma_3$$
$$- 0.0004114003724\sigma_1 + 0.0004114003724)\cos(0.3926990817x)^4$$
$$+ ((-3.321113337 \times 10^{-7}\sigma_1' - 1.974716484 \times 10^{-7}\sigma_3')$$
$$\times \sin(0.3926990817x) - 1.54985289 \times 10^{-6}\sigma_1' - 9.215343595 \times 10^{-7}$$
$$\times 10^{-7}\sigma_3')\cos(0.3926990817x)^3 + ((0.002523428571\sigma_1$$
$$+ 0.002524284342\sigma_3 - 0.002523428571)\sin(0.3926990817x)$$
$$+ 0.008228853414\sigma_1 + 0.008231064157\sigma_3 - 0.008228853414))$$
$$\times \cos(0.3926990817x)^2 + ((3.321113337 \times 10^{-6}\sigma_1' + 1.974716484$$
$$\times 10^{-6}\sigma_3')\sin(0.3926990817x) + 3.76392845 \times 10^{-6}\sigma_1'$$
$$+ 2.238012015 \times 10^{-6}\sigma_3')\cos(0.3926990817x) + (0.0136052106$$
$$- 0.0136052106\sigma_1 - 0.0136082058\sigma_3)\sin(0.3926990817x)$$
$$- 0.01448284969\sigma_1 - 0.01448593997\sigma_3 + 0.01448284969) \tag{B.5}$$

and D_2 is provided by

$$\begin{aligned} D_2 = {} & (0.02040816326\cos(0.3926990817x)^6 + (-2.81632653 \\ & - 0.3673469388\sin(0.3926990817x))\cos(0.3926990817x)^4 \\ & + (30.36734693 + 11.75510204\sin(0.3926990817x)) \\ & \times \cos(0.3926990817x)^2 - 42.44897958 - 41.14285714 \\ & \times \sin(0.3926990817x)). \end{aligned} \tag{B.6}$$

Appendix C. Validation

The developed analytical methodology is validated by comparing the analytical results with the numerical results from a finite element analysis in ABAQUS. A comparison of the normalized shear stress results from the analytical and numerical models, considering ungraded and single sinusoidal graded interphases is provided in Fig. C.1. The results from both models are observed to be in close agreement with each other.

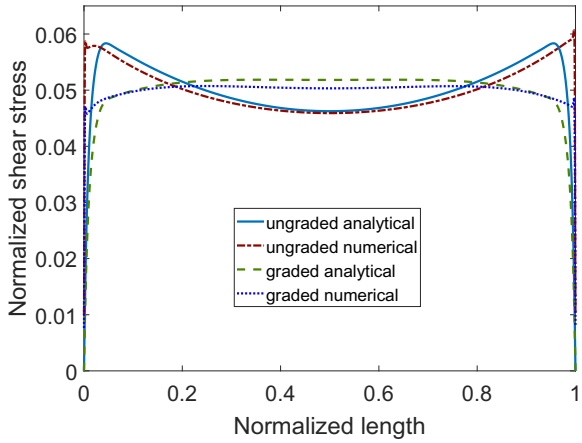

Fig. C.1. Comparison of the results from the analytical and numerical models, considering ungraded and sinusoidal graded interphases.

References

Ajayan, P., Braun, P. and Schadler, L. [2003] *Nanocomposite Science and Technology* (Wiley-VCH Verlag GmbH & Co. KgaA, Weinham, Germany).

Anitescu, C., Atroshchenko, E., Alajlan, N. and Rabczuk, T. [2019] "Artificial neural network methods for the solution of second order boundary value problems," *Comput. Mater. Contin.* **59**, 345–359.

Barthelat, F. and H. Espinosa [2007] "An experimental investigation of deformation and fracture of Nacre — mother of pearl," *Exp. Mech.* **47**, 311–324.

Budarapu, P., Kumar, S., Prusty, B. G. and Paggi, M. [2019] "Stress transfer through the interphase in curved-fiber pullout tests of nanocomposites," *Compos. Part B Eng.* **165**, 417–434.

Budarapu, P., Thakur, S., Kumar, S. and Paggi, M. [2020] "Micromechanics of engineered interphases in nacre-like composite structures," *Mech. Adv. Mater. Struct.* **28**(22), 2327–2342.

Carbas, R., Da Silva, L. and Andrés [2017] "Functionally graded adhesive joints by graded mixing of nanoparticles," *Int. J. Adhes. Adhes.* **76**, 30–37.

Carbas, R., Da Silva, L. and Critchlow, G. [2014] "Adhesively bonded functionally graded joints by induction heating," *Int. J. Adhes. Adhes.* **48**, 110–118.

Dusane, A., Budarapu, P., Pradhan, A., Natarajan, S., Reinoso, J. and Paggi, M. [2021] "Simulation of bridging mechanisms in complex laminates using a hybrid PF-CZM method," *Mech. Adv. Mater. Struct.* 1–29, https://doi.org/10.1080/15376494.2021.2006835.

Espinosa, H. D., Rim, J. E., Barthelat, F. and Buehler, M. J. [2009] "Merger of structure and material in nacre and bone — Perspectives on de novo biomimetic materials," *Prog. Mater. Sci.* **54**, 1059–1100.

Goland, M. and Reissner, E. [1944] "The stresses in cemented joints."

Goswami, S., Anitescu, C., Chakraborty, S. and Rabczuk, T. [2020] "Transfer learning enhanced physics informed neural network for phase-field modeling of fracture," *Theor. Appl. Fract. Mech.* **106**, 102447.

Guo, H., Zhuang, X., Chen, P., Alajlan, N. and Rabczuk, T. [2022] "Stochastic deep collocation method based on neural architecture search and transfer learning for heterogeneous porous media," *Eng. Comput.* 1–26, https://doi.org/10.1007/s00366-021-01586-2.

Hart-Smith, L. [1973] Adhesive-Bonded Single-Lap Joints.

Hongwei Guo, X. Z. and Rabczuk, T. [2019] "A deep collocation method for the bending analysis of Kirchhoff plate," *Comput. Mater. Contin.* **59**, 433–456.

Jackson, A., Vincent, J. F. and Turner, R. [1988] "The mechanical design of nacre," *Proc. Royal Soc. Lond. Ser. B* 234, 415–440.

Kawasaki, S., Nakajima, G., Haraga, K. and Sato, C. [2016] "Functionally graded adhesive joints bonded by honeymoon adhesion using two types of second generation acrylic adhesives of two components," *J. Adhes.* **92**, 517–534.

Khan, M. and Kumar, S. [2017] "Interfacial stresses in single-side composite patch-repairs with material tailored bondline," *Mech. Adv. Mater. Struct.* 1–15.

Khan, M. and Kumar, S. [2018] "Performance enhancement of tubular multilayers via compliance-tailoring: 3D printing, testing and modeling," *Int. J. Mech. Sci.* **140**, 93–108.

Khan, M., Kumar, S. and Reddy, J. [2018] "Material-tailored adhesively bonded multilayers: A theoretical analysis," *Int. J. Mech. Sci.* **148**, 246–262.

Kumar, S. [2009] "Analysis of tubular adhesive joints with a functionally modulus graded bondline subjected to axial loads," *Int. J. Adhes. Adhes.* **29**, 785–795.

Kumar, S., Wardle, B. L. and Arif, M. F. [2017] "Strength and performance enhancement of bonded joints by spatial tailoring of adhesive compliance via 3D printing," *ACS Appl. Mater. Interf.* **9**, 884–891.

Lubkin, J. and Reissner, E. [1955] "Stress distributions and design data for adhesive lap joints between circular tubes," American Society of Mechanical Engineers.

Nairn, J. [1997] "On the use of shear-lag methods for analysis of stress transfer in unidirectional composites," *Mech. Mater.* **26**, 63–80.

Nairn, J. [2001] "On the use of planar shear-lag methods for stress-transfer analysis of multilayered composites," *Mech. Mater.* **33**, 335–362.

Nairn, J. [2004] "Generalized shear-lag analysis including imperfect interfaces," *Mech. Mater.* **13**, 263–274.

Nguyen-Thanh, V. M., Anitescu, C., Alajlan, N., Rabczuk, T. and Zhuang, X. [2021] "Parametric deep energy approach for elasticity accounting for strain gradient effects," *Comput. Methods Appl. Mech. Eng.* **386**, 114096.

Ni, Y., Song, Z., Jiang, H., Yu, S. and He, L. [2015] "Optimization design of strong and tough nacreous nanocomposites through tuning characteristic lengths," *J. Mech. Phys. Solids* **81**, 41–57.

Oterkus, E., Barut, A., Madenci, E., Smeltzer, S. and Ambur, D. [2006] "Bonded lap joints of composite laminates with tapered edges," *Int. J. Solids Struct.* **43**, 1459–1489.

Pal, G. and Kumar, S. [2016] "Multiscale modeling of effective electrical conductivity of short carbon fiber-carbon nanotube-polymer matrix hybrid composites," *Mater. Des.* **89**, 129–136.

Samaniego, E., Anitescu, C., Goswami, S., Nguyen-Thanh, V. M., Guo, H., Hamdia, K., Zhuang, X. and Rabczuk, T. [2020] "An energy approach to the solution of partial differential equations in computational mechanics via machine learning: Concepts, implementation and applications," *Comput. Methods Appl. Mech. Eng.* **362**, 112790.

Sharma, S., Awasthi, R., Sastry, Y. S. and Budarapu, P. R. [2021] " Physics-informed neural networks for estimating stress transfer mechanics in single lap joints," *J. Zhejiang Univ. Sci. A* **22**, 621–631.

Stapleton, S. E., Waas, A. M. and Arnold, S. M. [2012] "Functionally graded adhesives for composite joints," *Int. J. Adhes. Adhes.* **35**, 36–49.

Stein, N., Mardani, H. and Becker, W. [2016] "An efficient analysis model for functionally graded adhesive single lap joints," *Int. J. Adhes. Adhes.* **70**, 117–125.

Sutrakar, V., Javvaji, B. and Budarapu , P. [2021] "Fracture strength and fracture toughness of graphene: MD simulations," *Appl. Phys. A* **127**, 1–11.

Ubaid, J., Wardle, B. L. and Kumar, S. [2018] "Strength and performance enhancement of multilayers by spatial tailoring of adherend compliance and morphology via multi-material jetting additive manufacturing," *Sci. Rep.* **8**, 1–10.

Van Pham, P., Mohareb, M. and Fam, A. [2018] "Finite element formulation for the analysis of multilayered beams based on the principle of stationary complementary strain energy," *Eng. Struct.* **167**, 287–307.

Varma, V., Yogeshwar Rao, R., Vundavilli, P., Pandit, M. and Budarapu, P. [2022] "A machine learning-based approach for the design of lower limb exoskeleton," *Int. J. Comput. Methods* 2142012, doi:10.1142/S0219876221420123.

Yacobi, B., Martin, S., Davis, K., Hudson, A. and Hubert, M. [2002] "Adhesive bonding in microelectronics and photonics," *J. Appl. Phys.* **91**, 6227–6262.

Zhuang, X., Guo, H., Alajlan, N., Zhu, H. and Rabczuk, T. [2021] "Deep autoencoder based energy method for the bending, vibration, and buckling analysis of Kirchhoff plates with transfer learning," *Eur. J. Mech. A/Solids* **87**, 104225.